Title	A new probabilistic long-period critical excitation procedure for isolated building structures
Author(s)	Bazrafshan, Arsalan; Khaji, Naser; Ahmadi, Goodarz
Citation	Mechanics Based Design of Structures and Machines , 52 (9) : 7063 - 7091
Issue Date	2024-01-03
DOI	
Self DOI	
URL	https://ir.lib.hiroshima-u.ac.jp/00056106
Right	This is an Accepted Manuscript of an article published by Taylor & Francis in Mechanics Based Design of Structures and Machines on 03 Jan 2024, available at: https://doi.org/10.1080/15397734.2023.2297242. This is not the published version. Please cite only the published version. この論文は出版社版ではありません。引用の際には出版社版をご確認、ご利用ください。
Relation	

A new probabilistic long-period critical excitation procedure for isolated building structures

Arsalan Bazrafshan[1], Naser Khaji*[2], Goodarz Ahmadi[3]

[1] *Faculty of Civil and Environmental Engineering, Tarbiat Modares University, P.O. Box 14115–397, Tehran, Iran*

[2] *Civil and Environmental Engineering Program, Graduate School of Advanced Science and Engineering, Hiroshima University, 1-4-1, Kagamiyama, Higashi-Hiroshima, Hiroshima 739-8527, Japan*

[3] *Department of Mechanical and Aerospace Engineering, Clarkson University, Potsdam, NY 13699-5725, USA*

Abstract

The present paper develops a new procedure for finding the most unfavorable long-period excitation for isolated building structures based on the probabilistic critical excitation method. The upper bound of earthquake input energy per unit mass is considered the problem's constraint, and a modified power spectral density (PSD) function is proposed to conform to the new constraint. It is shown that the new constraint can be used as a criterion to estimate the possible range of input energy of similar earthquakes. In addition, the new PSD function can control the excitation's intensity. Finally, three base-isolated shear buildings modeled as multi degree of freedom systems with nonproportional damping are considered, and the critical excitations for each model are found based on the proposed method. To examine the reliability of the results, three actual accelerograms with a considerably high level of total input energy are selected as benchmarks and linear dynamic analyses are conducted using these accelerograms along with the generated critical excitations. The results show that the generated long-period excitations can better estimate the structural behavior (i.e., maximum displacement, drift, and absolute acceleration of stories) than the actual benchmark accelerograms.

Keywords: Critical excitation, isolated building structures, non-stationary random process, total input energy per unit mass, synthetic accelerograms, long-period ground motions

Nomenclature

a	The lower limit of $\Delta\Omega$ as introduced in Eq. (20)
$A(\omega)$	The Fourier transform of the ground acceleration
$\overline{A}$	A pre-specified input parameter
$A_{Cj}(t,\omega)$	A function as introduced in Eq. (7)
$A_{Cj}^{*}(t,\omega)$	A function as introduced in Eq. (9)
$A_{Sj}(t,\omega)$	A function as introduced in Eq. (8)
$A_{Sj}^{*}(t,\omega)$	A function as introduced in Eq. (10)
b	The upper limit of $\Delta\Omega$ as introduced in Eq. (20)
$B_{Ck}^{(j)}(t,\omega)$	A function as introduced in Eq. (4)
$B_{Sk}^{(j)}(t,\omega)$	A function as introduced in Eq. (5)
$\mathbf{C}$	The viscous damping matrix of the system
$c(t)$	Envelope function
f	Objective function as introduced in Eq. (2)
g	Gravitational acceleration
$H(t_i,\omega)$	Rectangular PSD function
h_j	The undamped damping ratio of the jth mode
$H_N(t,\omega)$	A function as introduced in Eq. (3)
I_A	The Arias Intensity parameter
$\overline{I_A}$	A pre-specified input parameter
$\mathrm{Im}[\cdot]$	The imaginary part of the function inside the brackets
$\mathbf{M}$	The mass matrix of the system
n	Number of stories in a shear building
$\mathbf{r}$	Influence coefficient vector
$\mathrm{Re}[\cdot]$	The real part of the function inside the brackets
S_1	The value of S_w as introduced in Eq. (19)
S_2	The value of S_w as introduced in Eq. (19)
$S_w(\omega)$	The PSD function of $w(t)$
$\tilde{S}_w(\omega)$	The critical PSD function of $w(t)$
$\bar{S}_w$	The first constraint
$\bar{s}_w$	The second constraint

t_i	A certain time instant
$\mathbf{U}^{(j)}$	The jth damped complex eigenvector
$\ddot{u}_g(t)$	The input ground acceleration
$w(t)$	Stationary Gaussian random process
$\alpha_k^{(j)}$	A function as introduced in Eq. (6)
$\sigma_{D_k}(t)$	Interstory drift of the system
$\widetilde{\Omega}$	Specific frequency interval
Ω_L	The lower limit of the interval $\widetilde{\Omega}$
Ω_U	The upper limit of the interval $\widetilde{\Omega}$
$\Delta\Omega$	The width of the peak of the PSD function
ω_j	The undamped natural circular frequency of the jth mode
ω_{dj}	The damped natural circular frequency of the jth mode
ω_h	The maximum circular frequency of the excitation
ω_l	The minimum circular frequency of the excitation
CEM	Critical excitation method
MDOF	Multi degree of freedom
PSD	Power spectral density

1. Introduction

Seismic ground motions involve extensive inherent uncertainties, which make it difficult to predict future events (Zakian et al. 2017), which is necessary for seismic analysis (Semsar et al. 2023) and system identification (Pappalardo and Guida 2018) of various structures. Elastodynamics (Shafiei et al. 2020) demonstrates an extensive range of phenomena in physical and engineering problems, including fluid-soil-structure interaction (Moghadaszadeh and Khaji 2015; Babaee and Khaji 2020; Praharaj and Datta 2022; Kalantari and Khaji 2022), where wave propagation is represented by a set of governing linear partial differential equations, in conjunction with appropriate initial and boundary conditions. Along with the incredible increase in computational capacities, numerical methods have provided effective and robust forums to challenge wave propagation phenomenon to predict seismic ground motions (Khodakarami et al. 2012; Fujita and Ichimura 2016). In addition to numerical and analytical approaches to predict seismic ground motions (Ding et al. 2018; Rezaei et al. 2021), selection and/or generation of input seismic time history is another alternative as one of the most critical steps of the design process of structural systems, which involves some challenging issues (Bagheri et al. 2014; Hassani Sokhtesaraei et al. 2023; Matinfar et al. 2023; Wen et al. 2023). Numerous reliable methods have been developed to estimate these vital inputs during the past decades. Most of these methods employed in building codes are based on past observations. However, the existing data reflects a partial portion of the physical reality. On the other hand, considering the rapid increase in large structures, the effects of long-period ground motions should be given more attention and consideration (Cui et al. 2021; Durucan et al. 2021; Jian et al. 2022; Uenaga et al. 2023). In addition, the effects of base-isolation on the seismic response of fluid storage tanks (Shekari et al. 2010; Saha et al. 2014; Safari and Tarinejad 2018; Farajian et al. 2022) and buildings (Furinghetti et al. 2017; Mazza and Sisinno 2017; Sodha et al. 2017; Moeindarbari and Taghikhany 2018; Ye et al. 2019; De Domenico et al. 2020) subjected to long-period ground motions were studied in the literature. Long-period ground motions are generally divided into two types: long-period ground motions observed near faults and those observed far away from the source generated by large subduction-zone earthquakes and moderate to large crustal earthquakes in distant sedimentary basins (Koketsu and Miyake 2008; Ibrahim et al. 2016). Experiences of past earthquakes (e.g., Mexico City (1984), Kobe (1995), and Tohoku (2011)) clearly indicate that reliance on existing data will never resolve all related issues, and earthquakes are still unpredictable, even with present knowledge. Consequently, for the design of important and vital structures that are expected to remain functional after an earthquake, it is highly recommended to employ a worst-case analysis to consider the uncertainties of the ground motions. In other words, the structural design based on the critical excitation method (CEM) is a rational approach to overcome these issues. According to the CEM, each structure has its dynamic characteristics and should be designed for its critical input. This critical input is determined in such a manner that the desired quantity of the structure's response is maximized. The CEM provides efficient tools to determine such input.

The CEM has extensive literature over four decades. Drenick (1970) proposed the first critical excitation (CE) problem for a linear elastic single degree of freedom (SDOF) system with viscous damping. Srinivasan et al. (1991) extended Drenick's method to multi degree of freedom (MDOF) systems. Iyengar (1972) developed the

CEM for nonlinear systems. The CEMs for nonlinear systems have been extensively extended (Drenick 1977; Westermo 1985; Takewaki 2002; Au 2006; Moustafa 2009; Takewaki 2013; Akehashi and Takewaki 2021a; Akehashi and Takewaki 2021b; Akehashi and Takewaki 2021c; Takewaki and Akehashi 2021; Akehashi and Takewaki 2022), and various response parameters (e.g., ductility ratio, damage index, and reliability index) have been considered as objective functions (Abbas 2006; Abbas and Manohar 2007; Moustafa and Takewaki 2010; Moustafa 2011). Some researchers used different objective functions such as acceleration (Ahmadi 1979; Takewaki 2001c), earthquake input energy (Westermo 1985; Takewaki 2004), and earthquake energy input rate (Takewaki 2006). Iyengar and Manohar (1987) extended the concept of CE to stochastic problems. Takewaki (2001a) developed a new CEM for stationary and non-stationary random input using a stochastic index of response as the objective function. Based on this method, the CE is considered to have a rectangular power spectral density (PSD) function. The exciting point of Takewaki's method is its versatility in replacing the objective function or system properties without changing the overall procedure of the CEM.

According to a comprehensive literature review, to the authors' best knowledge, there is no research concerning the CEM for generating long-period critical excitations. Hence, it is worthwhile to examine the following two inquiries: (a) Can the CEM be implemented in earthquake engineering to generate the needed long-period critical strong ground motion time histories? (b) How should the existing CEM be modified to create a new version of CEM? The principal contribution of the present paper is to answer the above-raised questions. Despite all the efforts to develop various theoretically interesting methods of CEs, the main goal of such developments, which is putting it into practical application, is usually neglected. For example, it is challenging to find the rectangular PSD function for some objective functions, such as the acceleration response, because of the high-frequency fluctuations in the transfer function. On the other side, since the rectangular PSD function doesn't control the peak of the frequency content of the excitation, the method is only effective for generating narrowband excitations. The rectangular PSD function will unnecessarily include a wide range of unwanted frequencies near zero for long-period structures. The constraints of the problem are the other factors that need to be revised. They are imposed on quantities that are difficult to interpret physically. Furthermore, no guidelines are provided on determining these constraints or their upper limits. As a result, it is always possible to get worse results by increasing the constraint values. Lastly, due to the random nature of the excitation, a fixed value of constraints doesn't necessarily guarantee a critical response in the structure for all generated samples. A careful selection of objective functions and some modifications in the PSD function and the constraint are needed to overcome these challenges.

This paper aims to develop a new procedure to determine the CEs for base-isolated shear buildings, modeled as MDOF systems with nonproportional damping. Base-isolated buildings have been considered to show the method's capability to generate long-period excitations. Since the damping values of isolation systems are remarkable, the formulation of the problem for MDOF systems with nonproportional damping has been used, as presented by Takewaki (2001b). The selection of appropriate constraints is the main issue of using this method. It is shown that the upper bound of earthquake input energy per unit mass may be considered a suitable constraint for the present CE problem. This bound can be a reasonable benchmark to estimate the allowable range of input energy in similar earthquakes. It should be noted that Takewaki (2004) considered the total input energy as the objective function of the problem to determine its upper bound for any given earthquake time history. Since the single rectangular PSD function has many limitations and does not control the excitation's peak frequency, a new PSD function is proposed in this study, and its advantages are discussed. Finally, considering the proposed constraint and PSD function, the method determines the critical PSD functions for the models and generates the CEs.

The paper is organized as follows. Section 2 describes the mathematical principles and basic concepts of the CEM. Section 3 proposes the constraints of the problem. The proposed PSD function is demonstrated in Section 4. This is followed by presenting the numerical examples and discussing the results in Sections 5 and 6. Section 7 draws the conclusions.

2. The critical excitation problem

Consider an n-story shear building modeled as an elastic linear MDOF system with nonproportional damping, subjected to a non-stationary random base acceleration.

Input base acceleration is defined as the product of an envelope function $c(t)$ and a stationary Gaussian random process $w(t)$ with zero mean, as given by

$$\ddot{u}_g(t) = c(t)w(t). \tag{1}$$

The sum of the mean-square inter-story drift of the system can be obtained from the following equation (Takewaki 2001b)

$$f = \sum_{k=1}^{n} \sigma_{D_k}^2(t) = \int_{-\infty}^{+\infty} H_N(t,\omega)\, S_w(\omega) d\omega \tag{2}$$

where $S_w(\omega)$ is the PSD function of $w(t)$, and

$$H_N(t,\omega) = \sum_{k=1}^{n} \left[\left(\sum_{j=1}^{n} B_{Ck}^{(j)}(t,\omega) \right)^2 + \left(\sum_{j=1}^{n} B_{Sk}^{(j)}(t,\omega) \right)^2 \right] \tag{3}$$

in which

$$B_{Ck}^{(j)}(t,\omega) = \omega_{jd}\, \mathrm{Re}\left[\alpha_k^{(j)}\right] A_{Cj}^*(t,\omega) - \omega_{jd}\, \mathrm{Im}\left[\alpha_k^{(j)}\right] A_{Cj}(t,\omega) \tag{4}$$

$$B_{Sk}^{(j)}(t,\omega) = \omega_{jd}\, \mathrm{Re}\left[\alpha_k^{(j)}\right] A_{Sj}^*(t,\omega) - \omega_{jd}\, \mathrm{Im}\left[\alpha_k^{(j)}\right] A_{Sj}(t,\omega) \tag{5}$$

where ω_{dj} represents the damped natural circular frequency of the jth mode, and Re[·] and Im[·] denote the real and imaginary parts of the function inside the brackets. In addition,

$$\alpha_k^{(j)} = 2(U_k^{(j)} - U_{k-1}^{(j)}) \frac{\mathbf{U}^{(j)^{\mathrm{T}}}\mathbf{Mr}}{2(\omega_{dj} - \omega_j h_j)\mathbf{U}^{(j)^{\mathrm{T}}}\mathbf{MU}^{(j)} + \mathbf{U}^{(j)^{\mathrm{T}}}\mathbf{CU}^{(j)}} \tag{6}$$

in which $\mathbf{U}^{(j)}$ denotes the jth damped complex eigenvector, $\mathbf{M}$ and $\mathbf{C}$ indicate the mass and viscous damping matrices of the system, ω_j and h_j are the undamped natural circular frequency and damping ratio of the jth mode, and $\mathbf{r}$ implies the influence coefficient vector. Furthermore,

$$A_{Cj}(t,\omega) = \int_0^t c(\tau) e^{-h_j \omega_j (t-\tau)} \frac{1}{\omega_{jd}} \sin \omega_{jd}(t-\tau) \cos \omega\tau \, d\tau \tag{7}$$

$$A_{Sj}(t,\omega) = \int_0^t c(\tau) e^{-h_j \omega_j (t-\tau)} \frac{1}{\omega_{jd}} \sin \omega_{jd}(t-\tau) \sin \omega\tau \, d\tau \tag{8}$$

$$A_{Cj}^*(t,\omega) = \int_0^t c(\tau) e^{-h_j \omega_j (t-\tau)} \frac{1}{\omega_{jd}} \cos \omega_{jd}(t-\tau) \cos \omega\tau \, d\tau \tag{9}$$

$$A^*_{Sj}(t,\omega) = \int_0^t c(\tau)e^{-h_j\omega_j(t-\tau)}\frac{1}{\omega_{jd}}\cos\omega_{jd}(t-\tau)\sin\omega\tau\,d\tau \tag{10}$$

The critical excitation problem is now defined as follows: Given mass, stiffness, and nonproportional viscous damping matrices of a linear elastic MDOF system, as well as the envelope function, find the critical PSD function $\tilde{S}_w(\omega)$, to maximize the objective function f (see Eq. (2)) subject to the following constraints

$$\int_{-\infty}^{+\infty} S_w(\omega)d\omega \le \bar{S}_w \tag{11a}$$

$$\sup S_w\,(\omega) \le \bar{s}_w \tag{11b}$$

A simple solution is to consider $\tilde{S}_w(\omega)$ as a function with a constant value in a specific frequency interval. This interval is defined by the constraints of the problem as follows

$$\widetilde{\Omega} = \bar{S}_w/\bar{s}_w \tag{12}$$

This input is called the input with a rectangular PSD function (Takewaki 2001a). Using the rectangular PSD function, the objective function can be calculated as follows

$$f(t_i) = \bar{s}_w\int_{\Omega_L}^{\Omega_U} H(t_i,\omega)d\omega \tag{13}$$

where Ω_L and Ω_U are the upper and lower limits of the interval $\widetilde{\Omega}$ which specify the location of the rectangular PSD function. In a specific time of t_i, these parameters may be determined by vertically moving a horizontal line over the curve of the $H(t_i,\omega)$ function so that the distance between the intersection points reaches to $\widetilde{\Omega}$, as illustrated in Fig. 1. By repeating this procedure at different time steps t_i, the critical PSD functions are specified as rectangular functions, and the time history of the objective function is then determined. Finally, the PSD function corresponding to the objective function's maximum value is considered critical.

To solve the CE problem, the constraints should be first selected. According to Eq. (13), the objective function at the time t_i is obtained as the product of $\bar{s}_w$ and the area underneath the $H(t_i,\omega)$ function in the specific interval $\widetilde{\Omega}$. This means that the objective function is proportional to $\bar{s}_w$. Considering the concepts of $\bar{S}_w$ and $\bar{s}_w$, there is no straightforward way to recommend an appropriate value for these parameters. Consequently, it is difficult to estimate which value of $\bar{s}_w$ is sufficient to make the final non-stationary input critical. If a reasonable assumption can be made for the ratio of $\widetilde{\Omega} = \bar{S}_w/\bar{s}_w$, the method may be used to locate the rectangular function. However, for the applicability of the method, a new constraint should be considered, as proposed in the next section.

3. The constraints

Generally, all CE problems involve one (or more) constraint(s), which are essential to ensure that the presented excitation model is physically realistic and acceptable. However, the system's response significantly depends upon selecting these constraints. An inappropriate choice may lead to unrealistic or underestimated results. Therefore, it is necessary to consider a constraint that captures the actual situation.

By setting constraints on the ground motion's acceleration and velocity time histories, Takewaki (2004) determined an upper bound of total input energy per unit mass of a record for a damped linear elastic system. This bound is well-defined by two curves that perfectly bound the actual input energy curve in the range of short and long periods, as illustrated in Fig. 2. In this figure, the first curve entitled as "credible bound for acceleration constraint" is obtained by setting a constraint on the time integral of squared ground acceleration. This curve provides an overview of the possible total energy. This energy is then limited by the second curve, which is determined based on setting a similar constraint on the velocity of the ground motion in the range of long periods. This shows that the factors that cause changes in the velocity terms may lead to the generation of long-period ground motions. The two curves' intersection point may be considered the possible dominant period. However, the maximum actual input energy does not necessarily concentrate at this period.

In Takewaki's work (Takewaki 2004), the total input energy has been considered as the objective function of the problem to determine its upper bound for any given earthquake time history. On the contrary, in the present work, the total input energy has been effectively adopted as the constraint of the problem to find critical excitations with a certain upper bound of total input energy. This will introduce a rational base to the problem to ensure a realistic excitation model.

Investigations on the time history of various ground motions indicate that even for the same level of energy bound for acceleration constraint, the maximum amount of actual energy is not constant. Moreover, this maximum value may occur in different periods. Fig. 3 shows the total input energy of two various records of the 1979 Imperial Valley earthquake at stations 19 and 27 kilometers from the epicenter. As is observed from Fig. 3, the increase in distance does not lead to a significant drop in energy bound for acceleration constraint. In contrast, the bound of energy derived from the velocity constraint is substantially changed. Since the velocity credible bound has moved to the right, the energy content of the record is allowed to increase in the range of long periods, while the maximum of actual energy is approximately doubled. In other words, despite having an almost identical upper limit for acceleration constraint, the maximum amount of actual energy is changed for both value and position parameters, resulting in long-period ground motion. Such a situation can be observed in other earthquake records. Fig. 4 represents two samples of this situation. The characteristics of these ground motions are shown in Table 1. It is observed that even with almost the same magnitude, distance, and soil condition, as well as an identical upper bound for acceleration constraint, the energy content of records significantly varies.

These examples indicate that the upper bound of the total input energy for acceleration constraint can be used to estimate the allowable range for possible input energy in similar ground motions. As an earthquake is considered a non-stationary random process, existing ground motions represent a partial realization of the corresponding event. Therefore, relying on existing data could result in unsafe designs of critical structural systems. Now, consider a situation where the second long-period motion of Fig. 3 has not been recorded. In this case, proposing a method to find the worst realization/scenario of the same earthquake with a similar upper bound would be desirable. The upper bound of the input energy for acceleration constraint can be fully defined by the following two parameters

$$\int |A(\omega)|^2 d\omega \tag{14a}$$

$$\max|A(\omega)|^2 \tag{14b}$$

where $A(\omega)$ is the Fourier transform of the ground acceleration $\ddot{u}_g(t)$. Using Parseval's theorem, the integral of Eq. (14a) can be written as

$$\int |A(\omega)|^2 d\omega = 2\pi \int \ddot{u}_g^2(t) dt = 4gI_A \tag{15}$$

where g indicates the gravitational acceleration, and I_A is the well-known Arias Intensity parameter given by

$$I_A = \frac{\pi}{2g}\int \ddot{u}_g^2(t)dt \tag{16}$$

Therefore, to achieve a certain upper bound of the total input energy for acceleration constraint, the following constraints should be satisfied

$$I_A \leq \overline{I_A} \tag{17a}$$

$$\sup|A(\omega)| \leq \overline{A} \tag{17b}$$

where $\overline{I_A}$ and $\overline{A}$ are pre-specified input parameters, which can be easily selected based on the corresponding values of a target ground motion. The rectangular PSD function has a constant value for the interval of $\widetilde{\Omega}$. It is assumed that the interval of $\widetilde{\Omega}$ remains roughly unchanged after multiplying the random process $w(t)$ by the slowly varying envelope function $c(t)$. Consequently, a suitable approximation of this interval can be given as follows

$$\widetilde{\Omega} = \frac{4g\overline{I_A}}{\overline{A}^2} \tag{18}$$

To impose the constraints of Eq. (17), it is necessary to fix the peak of the Fourier transform $A(\omega)$ of the ground acceleration $\ddot{u}_g(t)$ as well as its Arias Intensity to pre-specified values. As illustrated earlier, $\ddot{u}_g(t)$ is defined as the product of an envelope function and a stationary Gaussian random process (see Eq. (1)). Due to the random characteristics of the problem, an iterative process is required to obtain the desired excitation with a certain Arias Intensity. To produce the non-stationary excitation, a band-limited stationary random approach is needed. However, as seen in Fig. 5a, the Fourier amplitude of such a process is entirely non-uniform with a wide range of variations. As the Arias Intensity of $\ddot{u}_g(t)$ is directly related to the area of its PSD function as indicated by Eq. (15), such variations can make it very difficult to satisfy the first condition. To resolve this problem, after generating the white noise process, the corresponding Fourier amplitudes are modified to achieve a rectangular shape, as depicted in Fig. 5b. This adjustment significantly facilitates obtaining the solution with considerably fewer iterations as it preserves the area of the PSD function.

To calculate the objective function, the maximum of the rectangular PSD function (i.e., $\bar{s}_w$) should be known (see Eq. (11)). In the conventional method, $\bar{s}_w$ is an input parameter of the problem. Conversely, by using the new constraint in this paper, it is not possible to determine $\bar{s}_w$ from the specified input parameter $\overline{A}$, because it is the maximum of the Fourier amplitude of the final nonstationary random process $\ddot{u}_g(t)$, rather than the initial stationary random process $w(t)$. Nevertheless, an initial estimation of the objective function can be obtained from Eq. (11), using an assumption for $\bar{s}_w$. At the same time, the final excitation can be simply scaled so that the maximum value of its Fourier amplitude is equal to the specified $\overline{A}$. As a result, the objective function is changed by this modification. However, it can be easily corrected to the initial estimation by multiplying the corresponding scale factor.

4. The PSD function

The single rectangular PSD function involves some limitations. First, since the rectangular PSD function does not control the excitation's peak frequency, the method is more efficient for the narrow-band target records. This will restrict the possible choices of target ground motions. Moreover, the simulated excitations generated based upon such PSD function would also have a narrow frequency content, which is not valid for most real earthquake records. The next problem appears when the fundamental period of the system is so long that the peak of the H_N function is located around zero. As may be discussed in the following sections, the base-isolated 14 and 20-story models examined in this paper have long fundamental periods, for which the peak of the H_N function is very close to zero. Since the $\widetilde{\Omega}$ determined from the target record is relatively large, the rectangular PSD function would have a wide range of frequencies near zero. Accordingly, the final excitation would have significant frequency content in very long periods (e.g., over 10 seconds). Such long-period excitations are not typically observed in the actual records.

The issues mentioned above may be fixed by using a piecewise function to define the PSD function rather than a single rectangular function, as follows

$$S_w = \begin{cases} 0; & \omega < \omega_l \\ S_1; & \omega_l < \omega < a \\ S_2; & a < \omega < b \\ S_1; & b < \omega < \omega_h \\ 0; & \omega_h < \omega \end{cases} \tag{19}$$

in which ω_l and ω_h are the minimum and maximum circular frequency of the excitation and $\Delta\Omega$ defines the width of the peak of the PSD function as given by

$$\Delta\Omega = b - a \tag{20}$$

Fig. 6 illustrates the schematic view of the new PSD function, in which parameters ω_l and ω_h introduce the frequency range of excitation. These parameters can be selected based on the frequency content of the target record. By choosing an appropriate value for ω_l, the frequency components of excitation near to zero areas (or very long periods) can be removed. Furthermore, by choosing a sufficiently small value for $\Delta\Omega$, the location of the peak of input energy for the generated excitation can be efficiently controlled. In addition, when the ratio of S_2/S_1 is large enough, the peak is more distinctive.

To completely determine the S_w function, a and b should be specified. While $\Delta\Omega$ can be arbitrarily selected as a constant value, a and b may be determined at any time t_i using the conventional method of moving the horizontal line over the plot of $H_N(t_i, \omega)$ function. Considering the original constraints of Eq. (11), when $S_2 = \bar{s}_w$ for any value of $\Delta\Omega$, then S_1 can be determined in such a way that the total area of PSD function, $\bar{S}_w$, remains the same. Therefore, one may write

$$S_1 = \frac{\bar{S}_w - \Delta\Omega.\bar{s}_w}{(\omega_h - \omega_l) - \Delta\Omega} \tag{21}$$

Using the new constraints given by Eq. (17), S_2 can be assumed as $\overline{A}^2$, and S_1 is then determined as follows:

$$S_1 = \frac{4g\overline{I_A} - \Delta\Omega.\overline{A}^2}{(\omega_h - \omega_l) - \Delta\Omega} \tag{22}$$

Any changes to $\Delta\Omega$ will be balanced by S_1, so that the area of the PSD function – and consequently the Arias Intensity of the critical excitation – does not change. Hence, there is no need to use only narrow-band target records.

The new method provides another advantage that allows reducing the final excitation's intensity. In many cases, the generated excitation based on a single PSD function leads to an unrealistically large response in the structural system. In the new method, $\Delta\Omega$ parameter can be used to decrease the intensity of the excitation. This feature is illustrated based on the definition of the objective function. To determine the objective function using the new PSD function, one may write

$$f = \int_{\omega_l}^{\omega_h} H_N(t,\omega) S_w(\omega) d\omega$$

$$= S_1 \int_{\omega_l}^{a} H_N(t,\omega) d\omega + S_2 \int_{a}^{b} H_N(t,\omega) d\omega + S_1 \int_{b}^{\omega_h} H_N(t,\omega) d\omega \qquad (23a)$$

$$= S_1 \int_{\omega_l}^{\omega_h} H_N(t,\omega) d\omega + (S_2 - S_1) \int_{a}^{b} H_N(t,\omega) d\omega = f_1 + f_2$$

where

$$f_1 = S_1 \int_{\omega_l}^{\omega_h} H_N(t,\omega) d\omega \qquad (23b)$$

and

$$f_2 = (S_2 - S_1) \int_{a}^{b} H_N(t,\omega) d\omega \qquad (23c)$$

By reducing $\Delta\Omega$ $(= b - a)$, the second term on the RHS of Eq. (23a) decreases. If the defined frequency range is sufficiently large, the increase of S_1 will not be sufficient to compensate for this reduction, and the objective function will decrease. Fig. 7a illustrates the general form of the objective function. As depicted in this figure, the second term of the f function has a small contribution to the objective function. Fig. 7b identifies the two different parts of the PSD function used to calculate f_1 and f_2. As mentioned in the previous section, to satisfy the second constraint as indicated by Eq. (17b), the final excitation should be scaled. This also leads to a change in the initial estimation of the objective function (see Eq. (13)). However, it can be simply corrected to the initial estimation by multiplying the corresponding scale factor. Appendix A presents a brief algorithm for the general procedure of the proposed method in this study and a demonstrative two-story shear building model.

5. Numerical examples

5.1. The objective function

In order to show the capability of the new method to control the intensity of the final excitation, an SDOF system with a natural period of 0.5(s) and a damping ratio of 0.02 is considered. To introduce the constraints, Manjil earthquake (Station Abhar, 327) with constraint parameters of $\overline{I_A} = 1.86$ (m/s) and $\overline{A} = 6.61$ (m/s) is selected as the target ground motion. This record is a reasonably narrow-band motion with a ratio of $\widetilde{\Omega} = 1.67$ (rad/s) as calculated from Eq. (18). Fig. 8 shows the upper bounds and the total input energy of the Manjil earthquake. With these constraints and using the envelope function illustrated in Fig. 9, the objective functions are found for different $\Delta\Omega$ including 1.67, 1.2, 0.9, 0.6, and 0.3 rad/s. The frequency range of the excitation is then controlled by setting $\omega_l = 0.5$ (rad/s) and $\omega_h = 19.5$ (rad/s). To obtain an initial estimation of the objective functions, S_2 can be assumed to be equal to $\overline{A}^2$. Fig. 10 draws the critical PSD functions for different values of $\Delta\Omega$. In addition, time histories of the objective functions are plotted in Fig. 11.

Based on the critical PSD functions of Fig. 10, five sample synthetic accelerograms are generated using the proposed new method, and the maximum displacement of the SDOF system is found using the linear time history analysis. Fig. 12 depicts the total input energy of generated excitations. Finally, Fig. 13. illustrates the total input energy of generated excitations versus the maximum displacement of the SDOF system.

5.2. The critical excitation

Numerical analyses are carried out using three typical shear buildings with 8, 14, and 20 stories mounted on the LRB base-isolators to examine the effect of long-period critical excitations on the structures. The buildings are designed as steel moment frames, for which the mass and stiffness of stories are then determined to be used for linear dynamic analyses of corresponding MDOF models. The isolation systems are designed based on the ASCE 7-10 recommendations. The isolation periods are considered 2.5 times the superstructure periods, which are equal to 0.81, 1.41, and 2.06 seconds, respectively. The basic characteristics of base-isolation systems are presented in Table 2.

Three actual ground motions corresponding to these models are used as benchmark records to find the critical excitation for the three models (see Fig. 14). Fig. 15 shows the critical PSD functions of the three models. Fig. 16 illustrates the corresponding time histories of the objective functions.

Fig. 17 depicts the time history of critical excitations generated based on the PSD functions. The total input energies of these accelerograms are drawn in Fig. 18.

Finally, Figs. 19 to 21 represent the maximum story displacement, superstructure drift, and absolute acceleration of benchmark records and their corresponding critical excitation responses.

6. Discussions

6.1. The objective function

As mentioned earlier, Fig. 10 shows the critical PSDFs for diverse values of $\Delta\Omega$. Note that the height of the PSD functions in this figure is represented schematically. As is seen in this figure, when $\Delta\Omega$ decreases, the corresponding S_1 value, determined from Eq. (22), increases to satisfy the first constraint of the problem, I_A. Also, the time histories of the objective functions plotted in Fig. 11 indicate that the objective function decreases as $\Delta\Omega$ becomes smaller.

Furthermore, Fig. 12 shows that a smaller value for the maximum total input energy to the natural period of the system is achieved using a smaller amount of $\Delta\Omega$. This reduction in the total input energy will reduce the maximum displacement of the system, as illustrated in Fig. 13.

6.2. The critical excitation

As stated, Fig. 14 represents the three real ground motions corresponding to the MDOF models. These motions have a considerably high level of total input energy at the first mode of each model and hence are assumed as "real critical excitations" for each model. In the actual situation, these records are unavailable, and the proposed method will be used to find them. However, the method is used here to regenerate real critical excitations. These records will be used to define the problem's constraints for each model. Additionally, these records are the basis for verification of the generated critical excitations. Using these ground motions and the generated critical excitations, linear dynamic analysis is conducted, from which the key parameters of the structural response (i.e., maximum displacement, drift, and acceleration of stories) are calculated and compared.

The input parameters of the PSD function are selected as 0.3, 0.5, and 30 (rad/s) for $\Delta\Omega$, ω_l and ω_h, respectively. These values ensure a wide range of frequencies and provide distinctive peaks of total input energy for the generated excitations. The problem's constraints, $\overline{I_A}$ and $\overline{A}$, are determined based on each ground motion, and the corresponding S_1 value is determined using Eq. (22). These parameters are listed in Table 3. The envelope function of the previous section will also be used here.

The critical PSDFs of three models are presented in Fig. 15, in which the height of the PSDFs is represented schematically. These PSDFs correspond to the peak of the objective functions. Also, it is observed from Fig. 16 that the shape of the objective function time histories has some fluctuation, resulting from considering complex modes and nonproportional damping. It is worth noting that solving the same problem without considering nonproportional damping will yield a smooth curve for the objective function. However, the critical PSD functions do not change. So, this additional computational effort seems to provide no extra accuracy for the current problem.

Because of its random nature, the accelerogram generated based on the PSD function may have different energy. However, to make comparisons between generated accelerograms and benchmark ground motions, the feasible records are those in which the input energy to the first mode of the models is more than the corresponding value of real records.

As seen from Fig. 17, unlike the single PSD function, which leads to narrow-band excitations and eliminates contributions of the higher modes, the generated accelerograms based on the new PSD function have a wide range of frequency content with more energy in the first mode's frequency of each model. Fig. 18 plots the total input energies of these accelerograms. These records have the same upper bound of energy for the acceleration constraint as the corresponding benchmark motions. Since the selected $\Delta\Omega$ is very small, the peak of the actual input energy is distinctive and concentrated at the models' natural period.

The structural responses, including the maximum story displacement, superstructure drift, and absolute acceleration of benchmark records and their corresponding critical excitation responses, are given in Figs. 19 to 21. The pattern of maximum displacement and drift of stories are similar in all cases. However, there are differences in the maximum absolute acceleration of stories. Absolute acceleration is directly related to the time history of base acceleration, while the produced excitations do not entirely match the actual records.

7. Conclusions

This study presented a new procedure for computing the most unfavorable long-period excitation for isolated building structures based on the CEM. The upper bound of earthquake input energy per unit mass was adopted as the problem's constraint. This constraint can be considered an appropriate parameter to estimate the possible range of total input energy in similar earthquakes. This bound introduces a class of ground motions for which the existing record is just one realization. Therefore, it is reasonable to fix the upper bound of input energy as the constraint of the CE problem and let the excitation change in amplitude and frequency content to maximize the objective function. In addition, a modified PSD function was proposed to conform to the new constraint. It was shown that the proposed constraint can be used as a criterion to estimate the possible range of input energy of similar earthquakes. Since the single rectangular PSD function does not provide control over the peak frequency of the excitation, a new PSD function was proposed in this paper. This PSD function can remove frequency contents near zero areas and provide a distinctive peak of input energy precisely at the natural period of the system. Moreover, choosing appropriate parameters for the PSD function reduces the intensity of the final excitation. Finally, three base-isolated shear buildings modeled as MDOF systems with nonproportional damping were considered, and the CEs for each model were found based on the proposed method. To examine the reliability of the results, three actual accelerograms with a considerably high level of total input energy were selected as benchmarks. Also, linear dynamic analyses of three models of base-isolated shear buildings were performed using these accelerograms along with the generated CEs. Comparison of the result of linear dynamic analysis under the CEs and three corresponding actual ground motions showed that the generated long-period CEs could estimate the behavior of structures (i.e., maximum displacement, drift, and absolute acceleration of stories) reasonably well – as if they were subjected to the actual ground motions.

In the present paper, the characteristics of the target earthquake (i.e., maximum Fourier amplitude and Arias Intensity) were used as constraints of the problem to generate critical excitations. This target earthquake can be the largest event that occurred in the vicinity of the site. Therefore, using a sample ground motion, other critical excitations can be generated with the same upper bound but different energy content.

Finally, it is worthwhile to remark that the proposed method should be developed for nonlinear systems, which the authors currently follow as a future study.

Acknowledgments: The authors would like to thank anonymous reviewers for their fruitful discussions and comments on the manuscript.

Appendix A

The CEM algorithm may be summarized as follows:

(i) Select the target record and compute the constraints using Eqs. (16) and (17).

(ii) Choose an appropriate value for ω_l, ω_h, and $\Delta\Omega$ and determine the S_1 value using Eq. (22). S_2 can be assumed equal to $\overline{A}^2$.

(iii) Apply the double maximization procedure as described in the original method:

  (a) Compute the transfer function $H_N(t, \omega)$ for a specific time $t = t_i$, using Eq. (3).

  (b) Determine the a and b using the original method of moving the horizontal line over the plot of $H_N(t_i, \omega)$ function.

  (c) Compute the objective function f, using Eq. (23a).

  (d) Repeat steps (a) through (c) for various times and find the $t = t_m$ for which the objective function f is maximized.

  (e) The PSD function for $t = t_m$ is determined as the critical one.

Given the critical PSD function, the CE may be generated by an iterative method as given below:

(i) A stationary random process is generated and modified to match the critical PSD function.

(ii) The non-stationary random process is then determined using Eq. (1) and scaled up to match the second constraint.

The procedure is repeated until the difference in the Arias Intensity of the excitation and that of the target record (i.e., the first constraint) falls within the acceptable tolerance.

A simple two-story shear building model is considered to demonstrate the procedure. The floor masses are assumed to be $m_1 = m_2 = 32000$ kg, and the story stiffnesses are $k_1 = k_2 = 820$ kN/m. These values are selected to provide a fundamental natural period of 2.0 second. The viscous damping coefficients of the building are $c_1 = c_2 = 54$ kN. s/m. The viscous damping matrix of the model is a proportional damping matrix where the lowest-mode damping ratio is almost equal to 0.1.

The Kobe earthquake (Kobe, JMA, 000) is selected as the target ground motion. The constraint parameters are determined as $\overline{I_A} = 8.38$ (m/s) and $\overline{A} = 5.83$ (m/s). $\tilde{\Omega}$

calculated from Eq. (18) equals 9.67 (rad/s), which is relatively large. As a result, the single rectangular PSD function will cover all frequencies from 0 up to 9.67 (rad/s), as shown in Fig. A1(a).

To use the new PSD function, a wide frequency range from $\omega_l = 1$ (rad/s) to $\omega_h = 50$ (rad/s) is set. This choice allows using a small value of $\Delta\Omega = 1$ (rad/s). Using Eq. (22), S_1 is calculated as 6.13. Also, S_2 can be assumed to be equal to $\overline{A}^2 = 33.99$. In the last step, the critical PSD function is determined using the double maximization procedure (see Fig A1(b)). A sample of critical excitation generated by this critical PSD function and its input energy, along with that of the target record, are illustrated in Fig. A2.

References

Abbas, A.M. 2006. Critical seismic load inputs for simple inelastic structures. Journal of Sound and Vibration 296:949–67.

Abbas, A.M., and C.S. Manohar. 2007. Reliability-based vector nonstationary random critical earthquake excitations for parametrically excited systems. Structural Safety 29:32–48.

Ahmadi, G. 1979. On the application of the critical excitation method to aseismic design. Journal of Structural Mechanics 7:55–63.

Akehashi, H., and I. Takewaki. 2021. Pseudo-double impulse for simulating critical response of elastic-plastic MDOF model under near-fault earthquake ground motion. Soil Dynamics and Earthquake Engineering 150:106887.

Akehashi, H. and I. Takewaki. 2022a. Bounding of earthquake response via critical double impulse for efficient optimal design of viscous dampers for elastic-plastic moment frames. Japan Architectural Review 5(2):131–49.

Akehashi, H. and I. Takewaki. 2022b. Pseudo-multi impulse for simulating critical response of elastic–plastic high-rise buildings under long-duration, long-period ground motion. The Structural Design of Tall and Special Buildings 31:e1969.

Akehashi, H. and I. Takewaki. 2022c. Resilience evaluation of elastic-plastic high-rise buildings under resonant long-duration ground motion. Japan Architectural Review 5(4):373–85.

Au, S.K. 2006. Critical excitation of SDOF elasto-plastic systems. Journal of Sound and Vibration 296:714–33.

Babaee, R., and N. Khaji. 2020. Decoupled scaled boundary finite element method for analysing dam–reservoir dynamic interaction. International Journal of Computer Mathematics 97:1725–43.

Bagheri, A., A.A. Fatemi, and G.G. Amiri. 2014. Simulation of earthquake records by means of empirical mode decomposition and Hilbert spectral analysis. Journal of Earthquake and Tsunami 8:1450002.

Cui, C., Y. Xu, and Z. Zeng. 2021. Mechanism study of vehicle–bridge dynamic interaction under near-fault ground motions. Journal of Earthquake and Tsunami 15:2150019.

De Domenico, D., Tubaldi, E., Takewaki, I., Karavasilis, T., Dall'Asta, A., & Lavan, O. (2020). Recent advances and applications of seismic isolation and energy dissipation devices. Frontiers in Built Environment 6:126.

Ding, Y., Y. Peng, and J. Li. 2018. A stochastic semi-physical model of seismic ground motions in time domain. Journal of Earthquake and Tsunami 12:1850006.

Drenick, R.F. 1970. Model-free design of aseismic structures. Journal of the Engineering Mechanics Division 96:483–93.

Drenick, R.F. 1977. The critical excitation of nonlinear systems. Journal of Applied Mechanics 44:333–36.

Durucan, C., H. Şahin, and A.R. Durucan. 2022. A new ground motion intensity measure for short period reinforced concrete structures subjected to near-fault pulse-like ground motions. Mechanics Based Design of Structures and Machines 51(4):2004–19.

Farajian, M., N. Saeed, and W.-H. Kang. 2022. Seismic vulnerability assessment of base isolated liquid storage tanks under near-fault ground motions. Structures 43:1901–12.

Fujita, K., and T. Ichimura. 2016. Development of large-scale three-dimensional seismic ground strain response analysis method and its application to Tokyo using Full K Computer. Journal of Earthquake and Tsunami 10:1640017.

Furinghetti, M., and A. Pavese. 2017. Equivalent uniaxial accelerogram for CSS-based isolation systems assessment under two-components seismic events. Mechanics Based Design of Structures and Machines 45 (3):282–95.

Hassani Sokhtesaraei, M., M. Ghassemieh, and S.R. Mirghaderi. 2023. Proposing a set of far-field records for time history analysis in Tehran city and comparison with FEMA-P695 set records. Journal of Earthquake and Tsunami 17:2250017.

Ibrahim, R., H. Si, K. Koketsu, and H. Miyake. 2016. Moment magnitude estimation of large earthquakes based on long-period ground motion prediction equations and preassumed fault models. Journal of Earthquake and Tsunami 10:1640004.

Iyengar, R.N. 1972. Worst inputs and a bound on the highest peak statistics of a class of non-linear systems. Journal of Sound and Vibration 25:29–37.

Iyengar, R.N., and C.S. Manohar. 1987. Nonstationary random critical seismic excitations. Journal of Engineering Mechanics 113:529–41.

Kalantari, M., and N. Khaji. 2022. Response of rigid circular plate in a functionally graded transversely isotropic, half-space under horizontal steady-state excitation. Mechanics Based Design of Structures and Machines (Article in Press) DOI: 10.1080/15397734.2022.2098762

Khodakarami, M.I., N. Khaji, and M.T. Ahmadi. 2012. Modeling transient elastodynamic problems using a novel semi-analytical method yielding decoupled partial differential equations. Computer Methods in Applied Mechanics and Engineering 213: 183–95.

Koketsu, K., and H. Miyake. 2008. A seismological overview of long-period ground motion. Journal of Seismology 12:133–43.

Matinfar, M., N. Khaji, and G. Ahmadi. 2023. Deep convolutional generative adversarial networks for generation of numerous artificial spectrum-compatible earthquake accelerograms using a limited number of ground motion records. Computer-Aided Civil and Infrastructure Engineering 38:225–40.

Mazza, F., and S. Sisinno. 2017. Nonlinear dynamic behavior of base-isolated buildings with the friction pendulum system subjected to near-fault earthquakes. Mechanics Based Design of Structures and Machines 45 (3):331–44.

Moeindarbari, H., and T. Taghikhany. 2018. Novel procedure for reliability-based cost optimization of seismically isolated structures for the protection of critical equipment: A case study using single curved surface sliders. Structural Control and Health Monitoring, 25(1), e2054.

Moghadaszadeh, S.O., and N. Khaji. 2015. Development and application of a semi-analytical method with diagonal coefficient matrices for analysis of wave diffraction around vertical cylinders of arbitrary cross-sections. Ocean Engineering 110:292–302.

Moustafa, A. 2009. Critical earthquake load inputs for multi-degree-of-freedom inelastic structures. Journal of Sound and Vibration 325: 532–44.

Moustafa, A. 2011. Damage-based design earthquake loads for single-degree-of-freedom inelastic structures. Journal of Structural Engineering 137:456–67.

Moustafa, A., and I. Takewaki. 2010. Characterization and modeling of near-fault pulse-like strong ground motion via damage-based critical excitation method. Structural Engineering and Mechanics 34:755–78.

Pappalardo, C.M., and D. Guida. 2018. System identification and experimental modal analysis of a frame structure. Engineering Letters, 26(1):56–68.

Praharaj, R. K., and N. Datta. 2022. Dynamic response of plates resting on a fractional viscoelastic foundation and subjected to a moving load. Mechanics Based Design of Structures and Machines 50 (7):2317–32.

Rezaei, M.H., N. Khaji, R. Di Maio, and A. Emolo. 2021. A modified Specific Barrier Model based on new time functions and approach for cracks location on the fault plane: Application to the 2008, Iwate-Miyagi earthquake. Geophysical Journal International 227:76–98.

Safari, S., and R. Tarinejad. 2018. Parametric study of stochastic seismic responses of base-isolated liquid storage tanks under near-fault and far-fault ground motions. Journal of Vibration and Control 24:5747–64.

Saha, S.K., V.A. Matsagar, and A.K. Jain. 2014. Earthquake response of base-isolated liquid storage tanks for different isolator models. Journal of Earthquake and Tsunami 8:1450013.

Semsar, S., S.R. Mirghaderi, F. Keshavarzi, and S. Ebrahimi. 2023. Improving the seismic performance of eccentrically braced frames using tie elements. Journal of Earthquake and Tsunami 17(4):2350013.

Shafiei, M., N. Khaji, and M. Eskandari-Ghadi. 2020. An adaptive cellular automata approach with the use of radial basis functions for the simulation of elastic wave propagation. Acta Mechanica, 231(7):2723–40.

Shekari, M.R., N. Khaji, and M.T. Ahmadi. 2010. On the seismic behavior of cylindrical base-isolated liquid storage tanks excited by long-period ground motions. Soil Dynamics and Earthquake Engineering 30:968–80.

Sodha, A.H., D.P. Soni, M.K. Desai, and S. Kumar. 2017. Behavior of quintuple friction pendulum system under near-fault earthquakes. Journal of Earthquake and Tsunami 11:1750017.

Srinivasan, M., B. Ellingwood, and R. Corotis. 1991. Critical base excitations of structural systems. Journal of Engineering Mechanics 117:1403–22.

Takewaki, I. 2001a. A new method for non-stationary random critical excitation. Earthquake Engineering and Structural Dynamics 30:519–35.

Takewaki, I. 2001b. Nonstationary random critical excitation for nonproportionally damped structural systems. Computer Methods in Applied Mechanics and Engineering 190:3927–43.

Takewaki, I. 2001c. Nonstationary random critical excitation for acceleration response. Journal of Engineering Mechanics 127:544–56.

Takewaki, I. 2002. Critical excitation for elastic–plastic structures via statistical equivalent linearization. Probabilistic Engineering Mechanics 17:73–84.

Takewaki, I. 2004. Bound of earthquake input energy. Journal of Structural Engineering 130:1289–97.

Takewaki, I. 2006. Probabilistic critical excitation method for earthquake energy input rate. Journal of Engineering Mechanics 132:990–1000.

Takewaki, I. 2013. Toward greater building earthquake resilience using concept of critical excitation: a review. Sustainable Cities and Society 9:39–53.

Takewaki, I. and H. Akehashi. 2021. Comprehensive review of optimal and smart design of nonlinear building structures with and without passive dampers subjected to earthquake loading. Frontiers in Built Environment 7:631114.

Uenaga, T., P. Omidian, R.C. George, M. Mirzajani, and N. Khaji. 2023. Seismic resilience assessment of curved reinforced concrete bridge piers through seismic fragility curves considering short- and long-period earthquakes, Sustainability, 15(10):7764.

Wen, P., B. Zhou, and R. Wen. 2023. Conditionally simulated nonstationary multi-point earthquake accelerograms using regressive model. Journal of Earthquake and Tsunami 17(5):2350020.

Westermo, B.D. 1985. The critical excitation and response of simple dynamic systems. Journal of Sound and Vibration 100:233–42.

Ye, K., Y. Xiao, and L. Hu. 2019. A direct displacement-based design procedure for base-isolated building structures with lead rubber bearings (LRBs). Engineering Structures, 197:109402.

Yu, J., L. Jiang, W. Zhou, X. Liu, Z. Lai, and Y. Feng. 2022. Study on the dynamic response correction factor of a coupled high-speed train–track–bridge system under near-fault earthquakes. Mechanics Based Design of Structures and Machines 50 (9): 3303–21.

Zakian, P., N. Khaji, and M. Soltani. 2017. A Monte Carlo adapted finite element method for dislocation simulation of faults with uncertain geometry. Journal of Earth System Science 126:1–22.

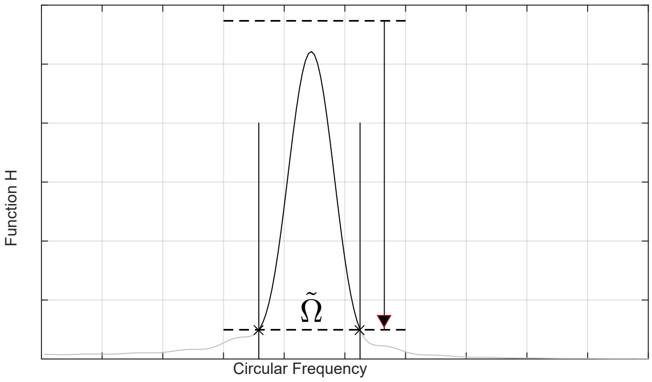

Fig. 1. Schematic diagram of the procedure for finding the critical PSD function as a rectangular function (adopted from Takewaki, 2001b).

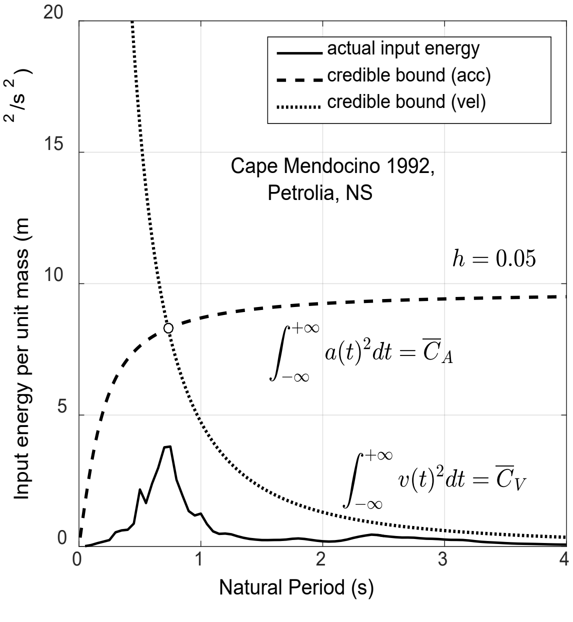

Fig. 2. Illustration of upper bounds and actual input energy of the 1992 Cape Mendocino earthquake (adopted from Takewaki, 2004).

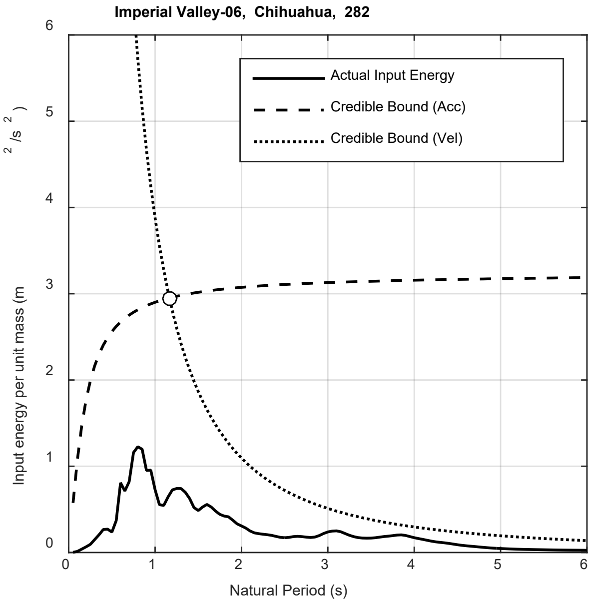

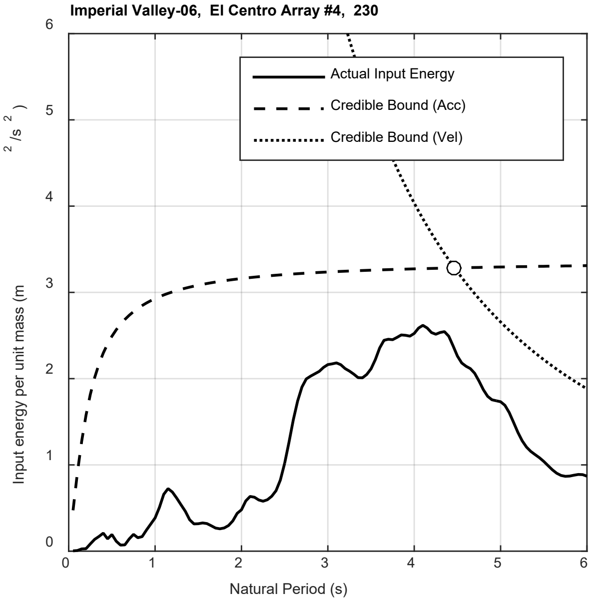

Fig. 3. Total input energy of two different records of the 1979 Imperial Valley earthquake.

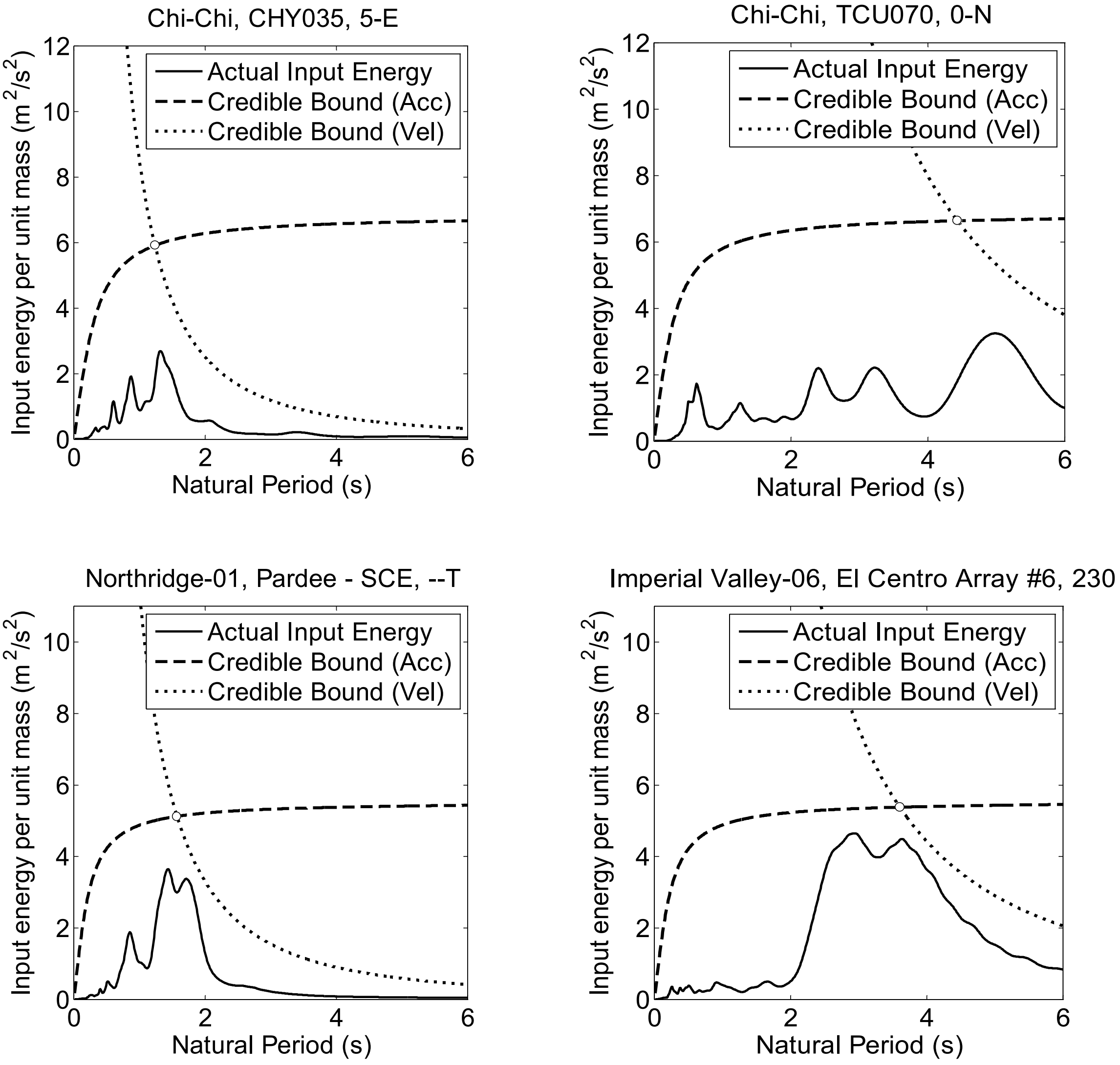

Chi-Chi, CHY035, 5-E

Chi-Chi, TCU070, 0-N

Northridge-01, Pardee - SCE, --T

Imperial Valley-06, El Centro Array #6, 230

Fig. 4. Examples of total input energy for different earthquakes with the same upper bound of energy for acceleration constraint.

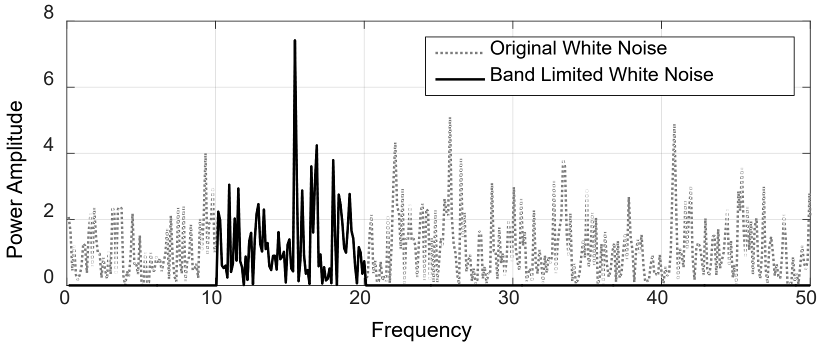

(a)

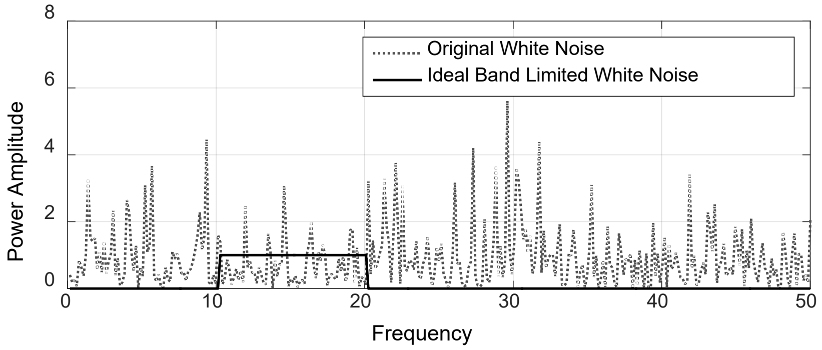

(b)

Fig. 5. Comparison of the PSD function of (a) original and (b) modified band-limited white noises.

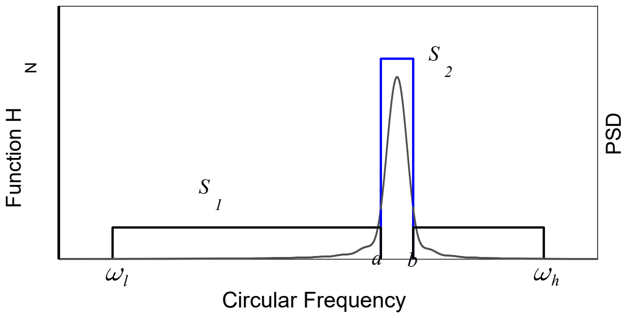

Fig. 6. Schematic view of the new PSD function.

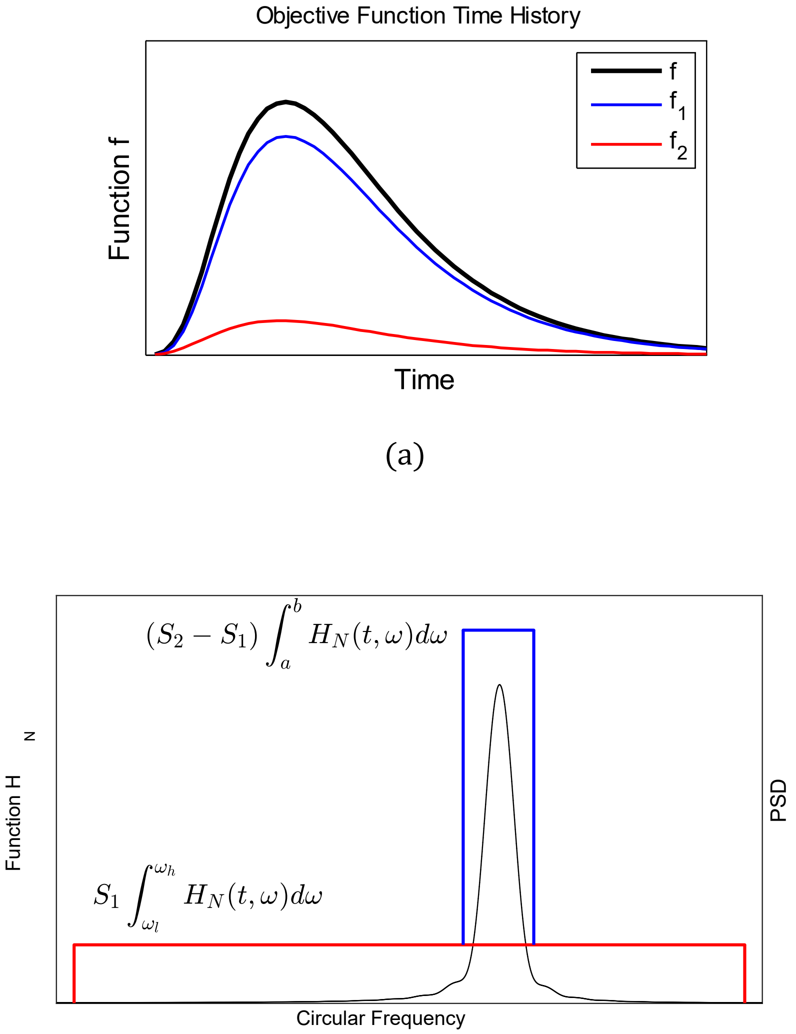

(a)

(b)

Fig. 7. Illustration of the objective function; (a) general form, and (b) contribution of integrals in H_N.

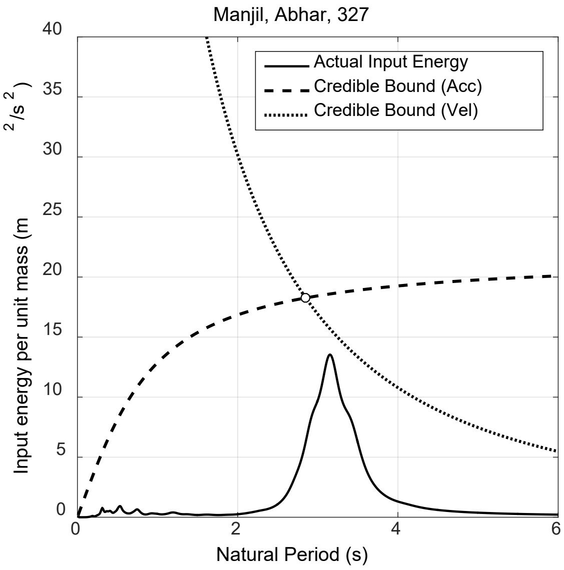

Fig. 8. The total input energy of the target record.

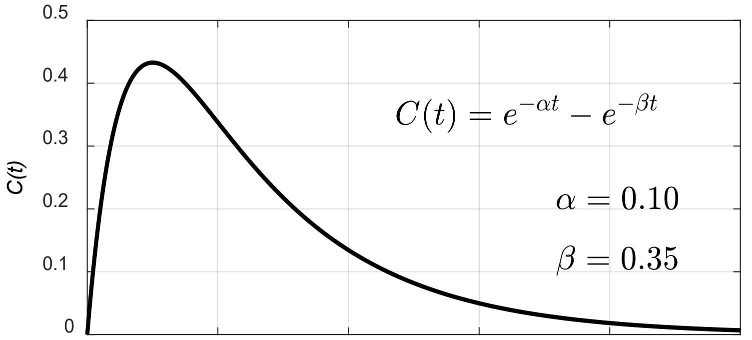

Fig. 9. The envelope function used for the illustrative SDOF model.

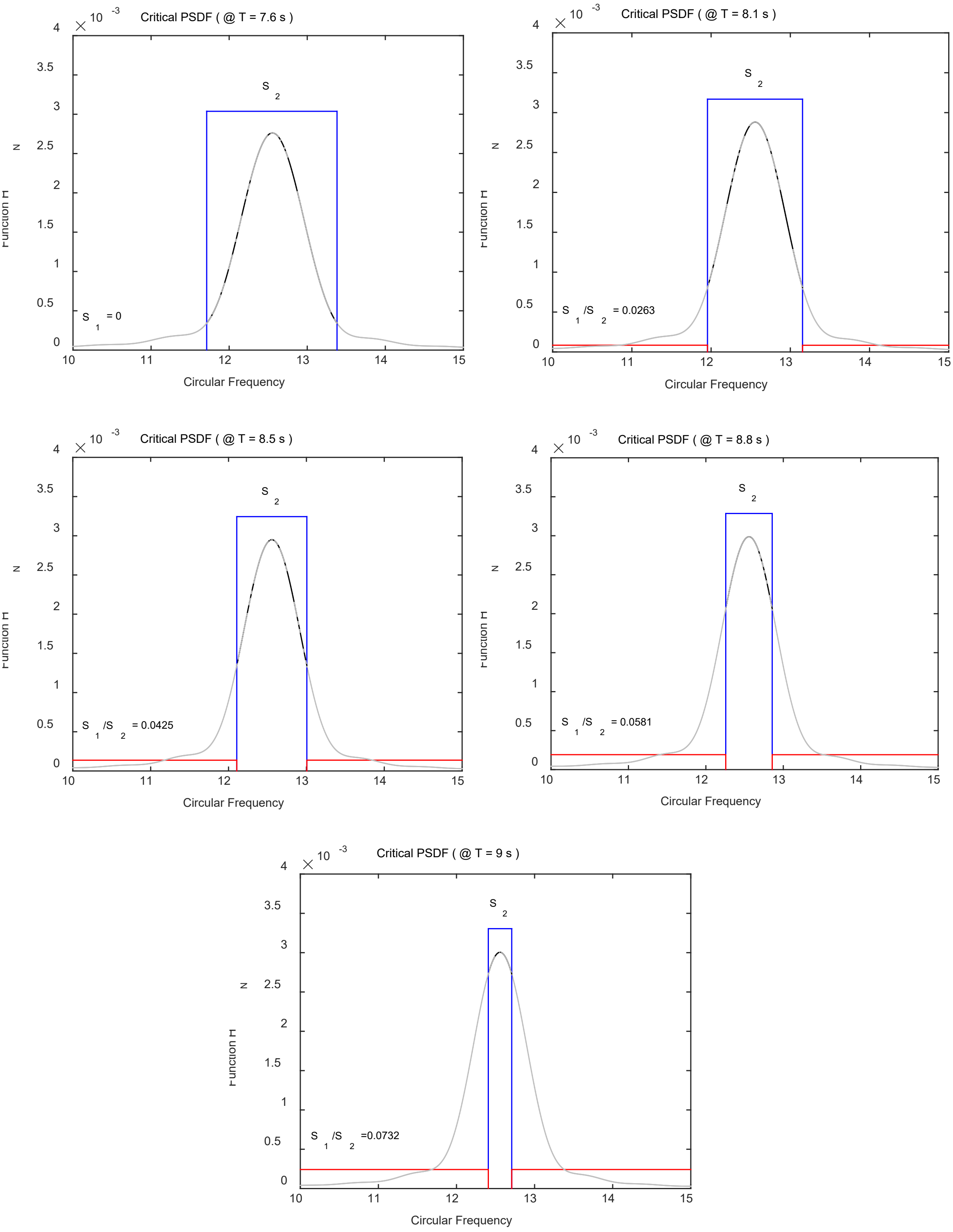

Fig. 10. Critical PSD functions (PSDFs) for five various values of the period as indicated in the parentheses.

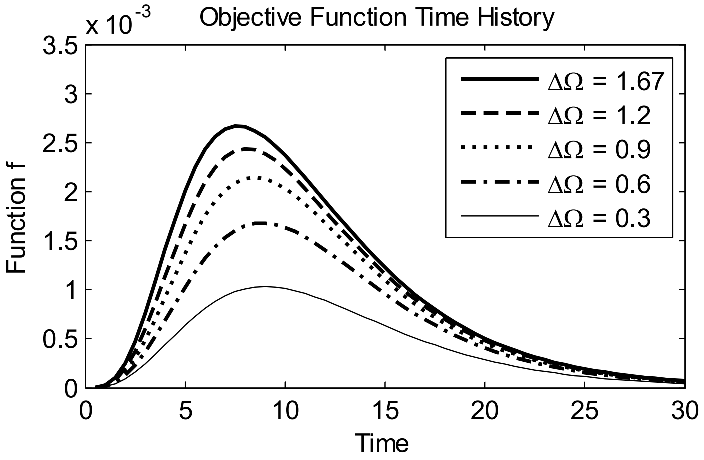

Fig. 11. Variation of initial objective functions of the SDOF model for various ΔΩ parameters.

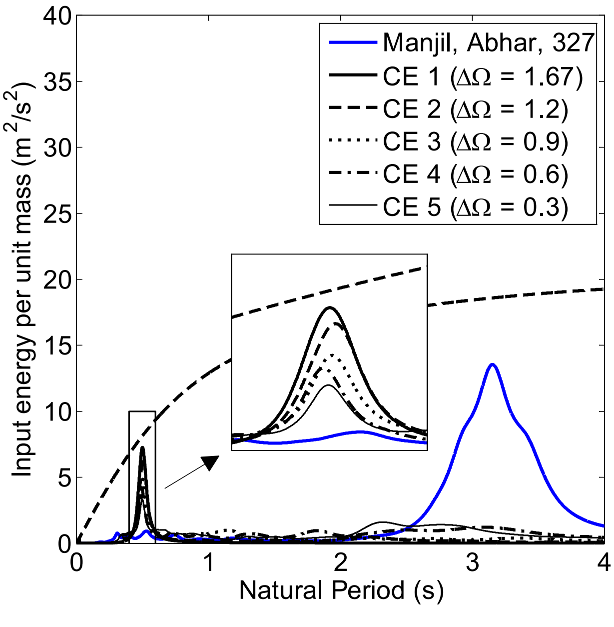

Fig. 12. The total input energy of the target record as well as generated excitations.

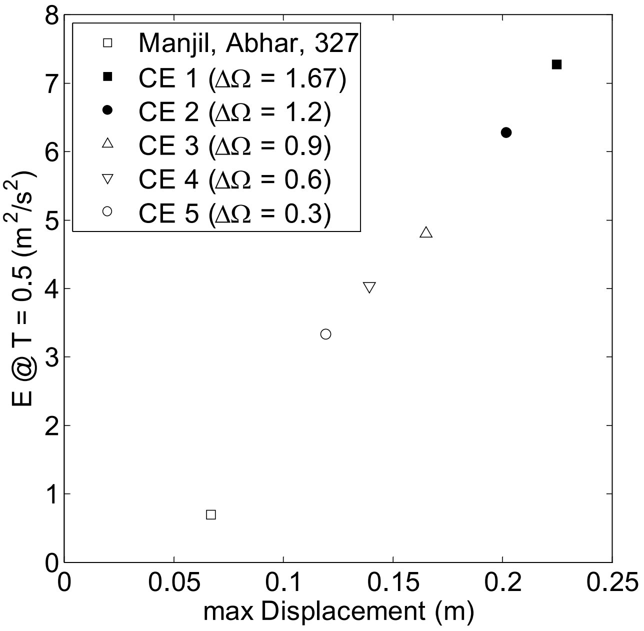

Fig. 13. Plot of total input energy of generated excitations versus the maximum displacement of the SDOF system.

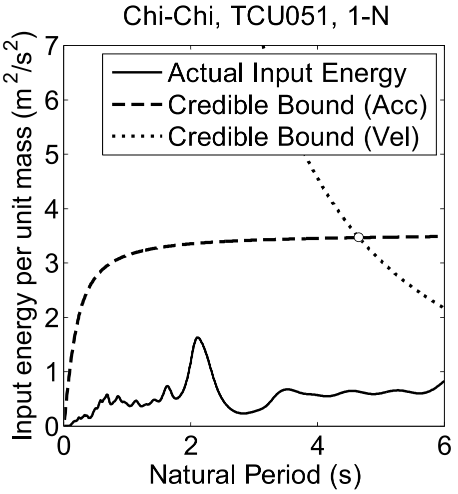

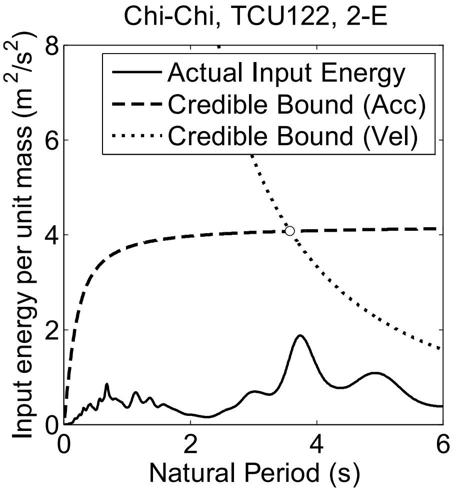

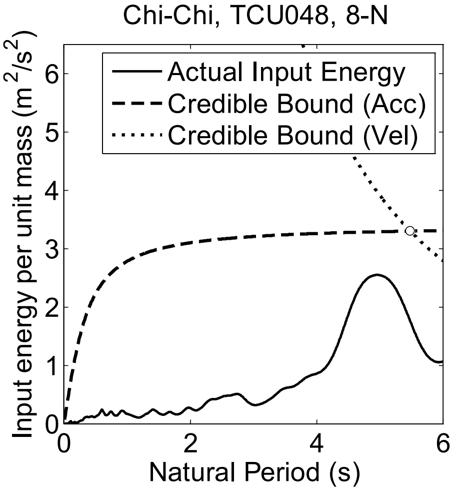

Fig. 14. Total input energies of the selected ground motions.

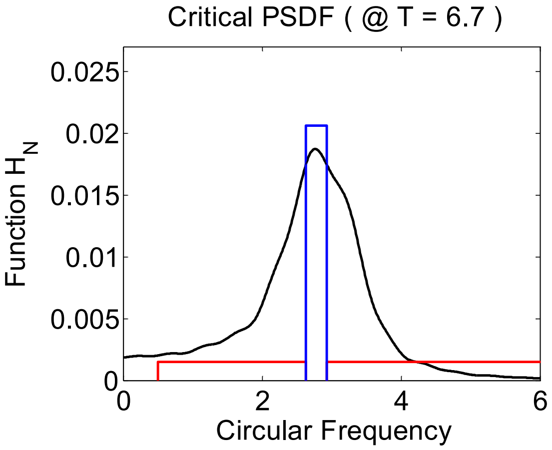

(a)

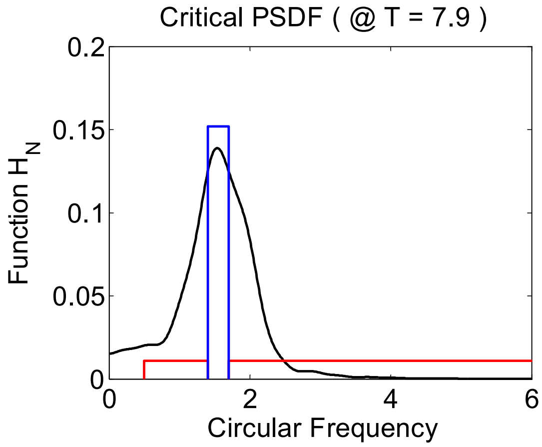

(b)

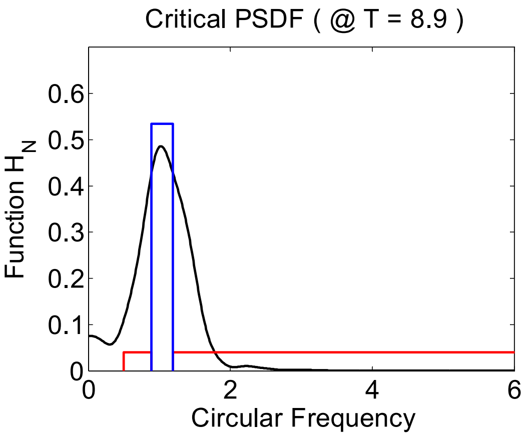

(c)

Fig. 15. Critical PSD functions (PSDFs) corresponding to the peak of objective functions of (a) 8-story, (b) 14-story, and (c) 20-story base-isolated shear buildings.

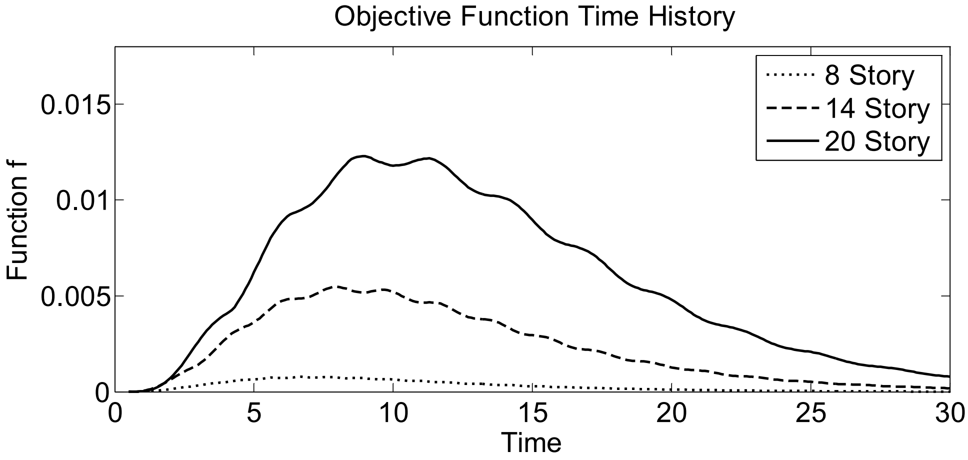

Fig. 16. Time histories of the objective functions for the three models.

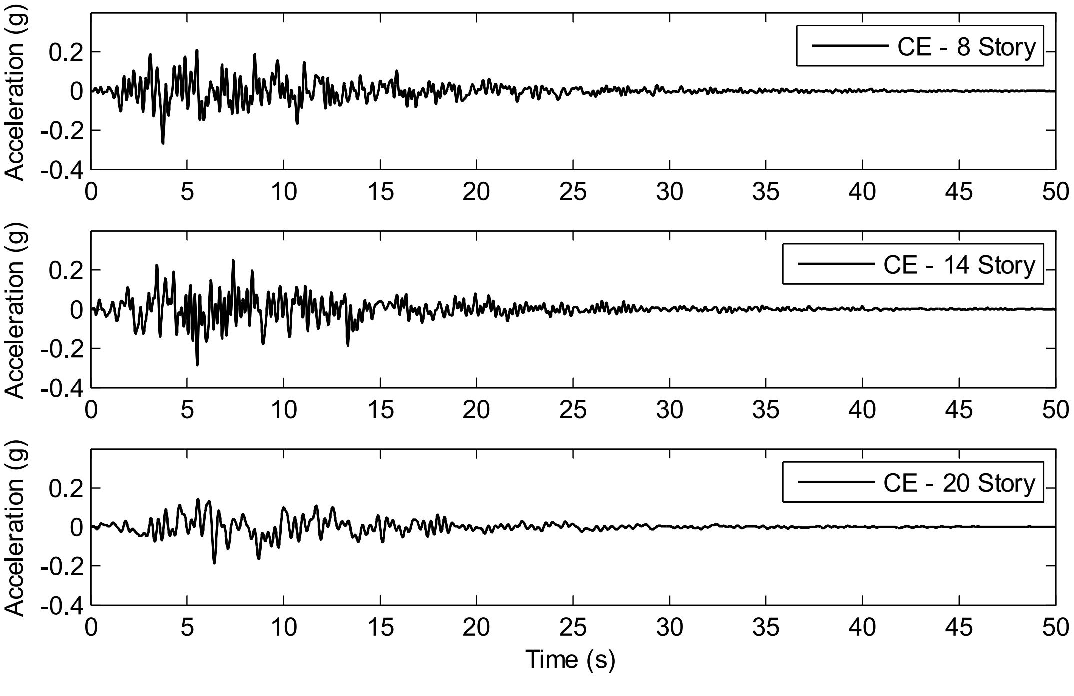

Fig. 17. Time histories of generated critical excitations.

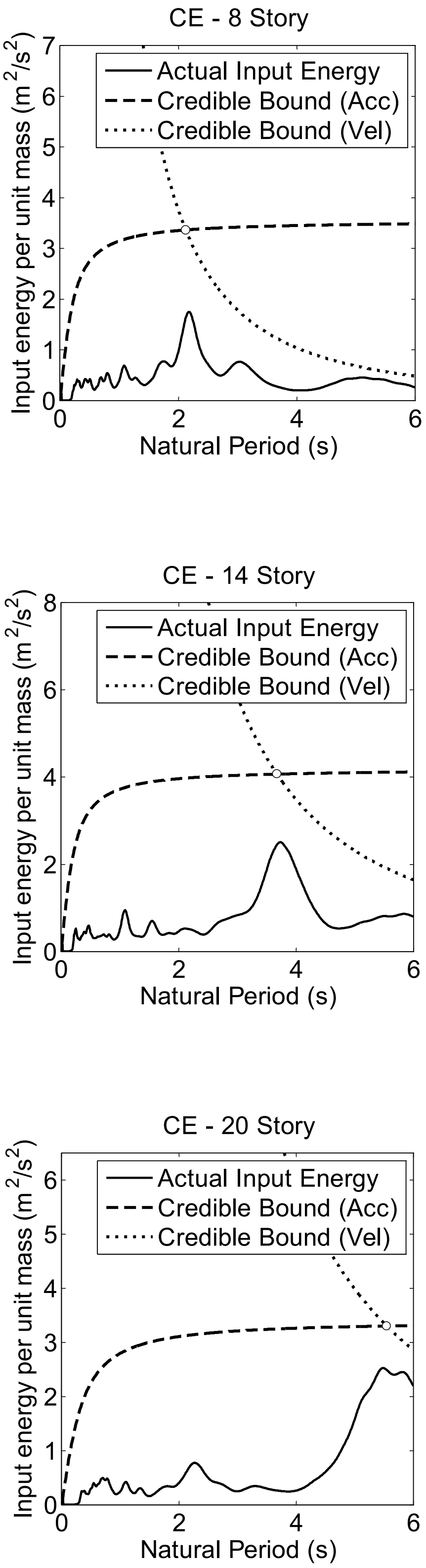

Fig. 18. Total input energies of generated critical excitations.

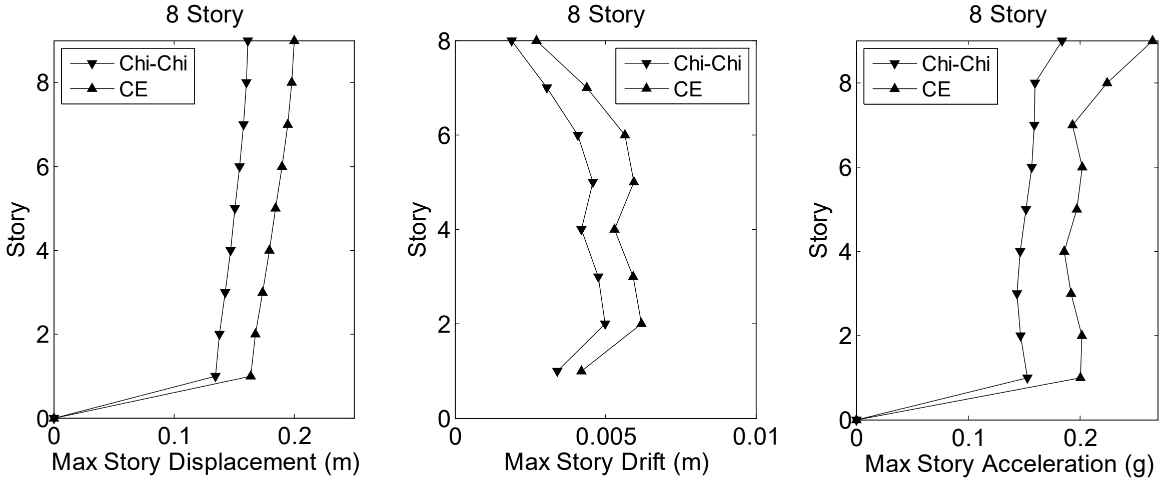

(a) (b) (c)

Fig. 19. (a) Maximum displacement, (b) maximum inter-story drift, and (c) maximum absolute acceleration of the 8-story model.

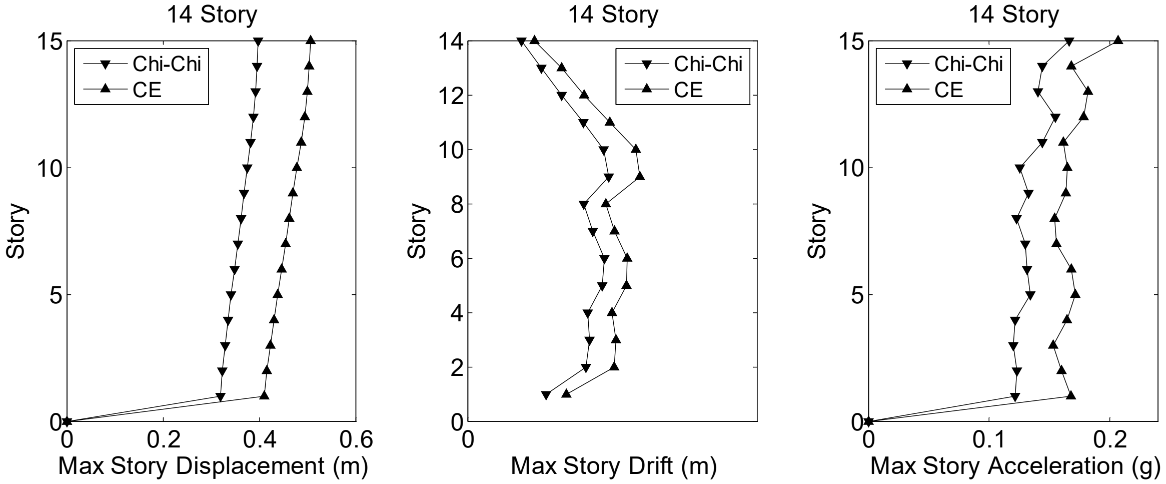

(a) (b) (c)

Fig. 20. (a) Maximum displacement, (b) maximum inter-story drift, and (c) maximum absolute acceleration of the 14-story model.

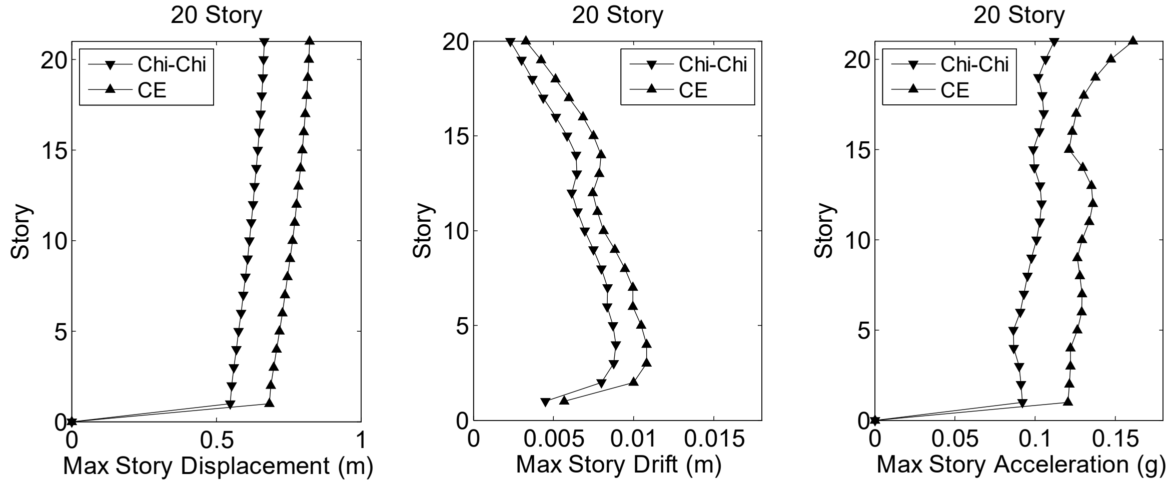

(a) (b) (c)

Fig. 21. (a) Maximum displacement, (b) maximum inter-story drift, and (c) maximum absolute acceleration of the 20-story model.

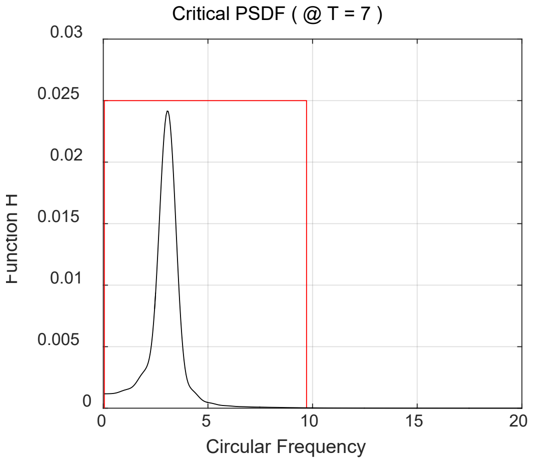

(a)

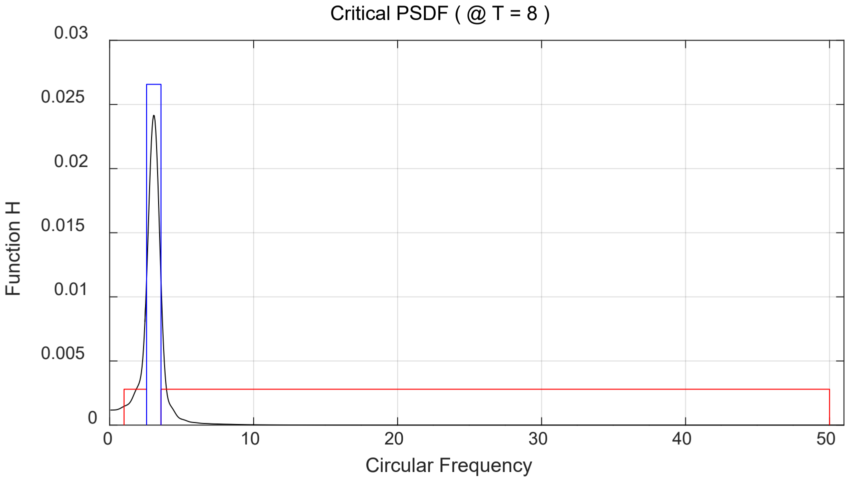

(b)

Fig. A1. (a) Single rectangular PSD Function assigns constant amplitude to the whole frequency range and includes unwanted low frequencies for long-period structures. (b) The new PSD function fully controls the frequency range and the peak. Note that the height of the PSD functions in this figure is represented schematically.

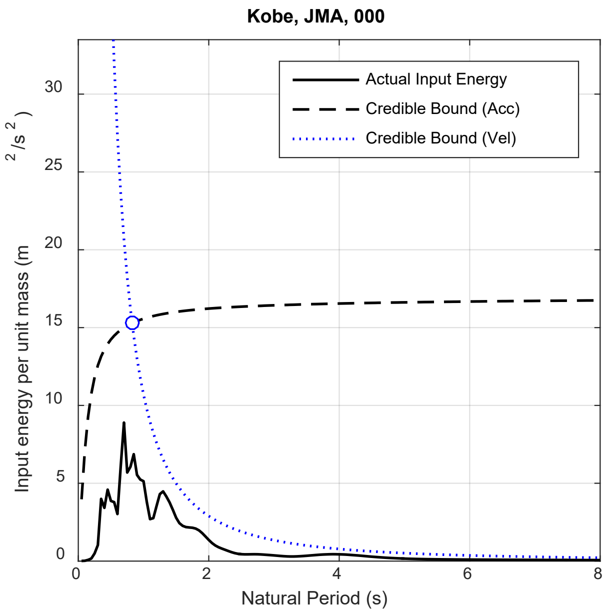

(a)

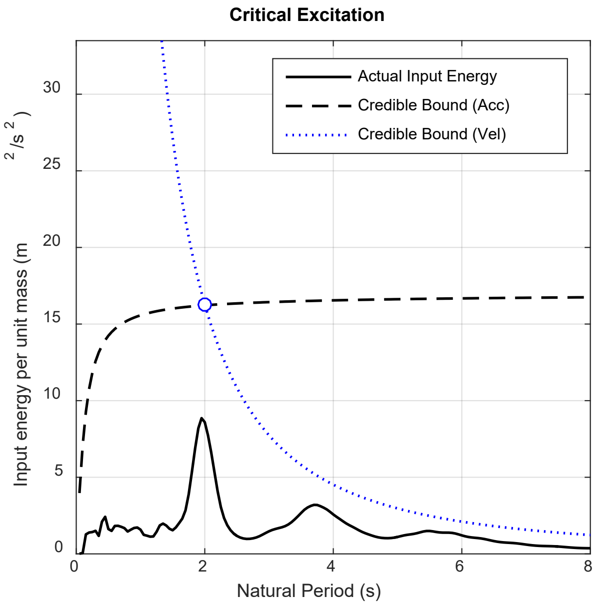

(b)

Fig. A2. (a) Illustration of input energy per unit mass for the target record, and (b) a sample CE (b). A CE with a wide range of frequencies can be generated using the new PSD function. It can be seen that the peaks of total input energy have been effectively transferred to the fundamental period of the structure while preserving the upper bound constraint (dashed line).

Table 1. Characteristics of sample ground motions of Fig. 4.

Event	Station	Component	Magnitude	Epicentral distance (km)	Soil type	V_{S30} (m/s)
Chi-Chi	CHY035	5-E	7.62	43.9	C	473
Chi-Chi	TCU070	0-N	7.62	47.9	C	401
Northridge	Pardee - SCE	--T	6.69	25.7	D	345
Imperial Valley	El Centro Array #6	230	6.53	27.5	D	203

Table 2. Basic characteristics of base-isolation systems

Parameter	8-story	14-story	20-story
T_{eff} (s)	2.02	3.54	5.14
h_{eff} (%)	16.5	16.1	15.8
D_D (cm)	21	37	54

Table 3. Characteristics of the selected ground motions.

Event	$\overline{I_A}$	$S_2 = \overline{A}^2$	S_1
Chi-Chi, TCU051, 1-N	1.182	7.178	1.5139
Chi-Chi, TCU122, 2-E	1.438	8.5	1.8445
Chi-Chi, TCU048, 8-N	0.714	6.898	0.8885